Predictive 3D modelling of free oblique cutting with an ANN-based material constitutive model and experimental validation over a wide range of conditions

F. Ducobu[a,*], O. Pantalé[b], B. Lauwers[c]

[a] *Machine Design and Production Engineering Lab, Research Institute for Science and Material Engineering, UMONS, Belgium*
[b] *Laboratoire Génie de Production, INP/ENIT, Université de Toulouse, Tarbes, France*
[c] *Department of Mechanical Engineering, KU Leuven & Flanders Make@KU Leuven-MaPS, Belgium*

Abstract

Modelling of the cutting process needs to move from 2D to 3D configurations to get closer to industrial applications. This study introduces a predictive 3D finite element model of free orthogonal and oblique cutting with an ANN-based material constitutive model and experimental validation in strictly the same conditions (cutting and geometrical). The developments are applied to the formation of continuous chips for the titanium alloy Ti6Al4V and an unseen broad range of 36 cutting conditions is considered: 2 cutting edge inclinations, 3 uncut chip thicknesses and 6 cutting speeds. The predictive performance of the model (i.e., the evaluation of the trends of fundamental variables with the absence of tuning of both numerical parameters and model features when cutting conditions are significantly modified) is high for the forces, mainly cutting and passive, and the chip thickness ratio on all 36 cutting conditions. The accuracy of the main cutting force is excellent: the mean difference with the experiments is 4%, within the experimental dispersion. No significant degradation of the results is brought by the apparition of the third, out-of-plane, force, which shows the ability of the model to handle orthogonal and oblique cutting configurations.

[FD:] Add a comment on ANN?

Keywords:

*Corresponding author. Tel.: +32 65 45 68
Email address: `Francois.Ducobu@umons.ac.be` (F. Ducobu)

Oblique cutting, Finite element method (FEM), Predictive model, Artificial Neural Network (ANN)

1. Introduction

Selection of the tools and the cutting conditions in machining, but also comprehension of the influence of the process parameters on the quality of a component and its optimization, are still difficult to achieve because of the high level of complexity and linked nonlinear phenomena. In the frame of digital manufacturing and Industry 4.0, modelling the cutting process supports them, while remaining a challenging task. As highlighted by Arrazola et al. [1], most finite element (FE) models are developed in 2D (orthogonal cutting configuration usually) although industrial applications require 3D modelling.

Experimental validation of a model is a crucial step in the modelling of the cutting process. The experimental configuration must be as close as possible to the simulation. For orthogonal cutting validation, a rotating movement usually generates the cutting speed. This is often achieved in turning [2] or in milling [3] and the diameter of the rotating part must be large enough to reduce the influence of the curvature on the results. Experimental configurations in strictly orthogonal cutting conditions are less often adopted, for example, on broaching [4] or milling [5, 6] machines. While they remove assumptions linked to the rotating cutting movement, they usually allow for lower cutting speeds (except on a dedicated machine, such as in Afrasiabi et al. [7]). Free oblique cutting with a straight cutting edge has not been studied yet: all the efforts have been focussing on orthogonal cutting (mostly for 2D validation).

Lagrangian and Eulerian formulations are the most used for FE modelling of the cutting process. Combinations of formulations, such as Arbitrary Lagrangian-Eulerian (ALE) and Coupled Eulerian-Lagrangian (CEL) are increasingly used to avoid (or reduce) mesh distortions [8]. The Coupled Eulerian-Lagrangian (CEL) formulation has recently been successfully applied to the modelling of cutting (2D orthogonal configuration): it provides accurate results with a realistic chip shape and no mesh distortion [8]. First applications in 3D are found in recent works [3, 9–12]. They cover (free) orthogonal cutting or a simple 3D operation, while free oblique cutting still needs to be investigated.

The behaviour of the machined material is one of the key aspects of a FE model [1, 13]. Research is very intense in this field, which leads to a growing number of material constitutive models ranging from empirical to physical models, some including microstructure effects [13]. The thermo-elasto-viscoplastic empirical model of Johnson-Cook (JC) [14] is still the most used so far:

$$\sigma^y = \left(A + B\,\varepsilon^{p^n}\right)\left(1 + C\ \ln\frac{\dot{\varepsilon}^p}{\dot{\varepsilon}_0^p}\right)\left(1 - \left[\frac{T - T_{\mathrm{room}}}{T_{\mathrm{melt}} - T_{\mathrm{room}}}\right]^m\right) \tag{1}$$

In this model, the flow stress, σ^y, is a function of the plastic strain, ε^p, of the plastic strain rate, $\dot{\varepsilon}^p$, and of the temperature, T. It is composed of 3 terms describing independently plastic, viscous and thermal aspects. One of the points in favour of its adoption is the rather limited number of parameters to be identified, 5: A, B, C, m and n. $\dot{\varepsilon}_0^p$ is the reference plastic strain rate, while T_{room} and T_{melt} are the room temperature and the melting temperature, respectively. More recent models developed based on it, such as the one of Calamaz et al. [15], increase this number of parameters (for Calamaz's particular model to 9). The better (in theory) description of the behaviour is achieved at the cost of a greater complexity of the identification process and of a reduction of the link with the physical meaning of the model.

One issue of material behaviour modelling for cutting simulation is the identification of the parameters, moreover, as the experimental equipment does not allow to reach the high levels of strains, strain rates and temperature of machining [13]. Inverse identification is an alternative, but the uniqueness of the solution is not always guaranteed [1, 13]. The early work of Özel and Altan [16] used the least squares method to inversely identify the input parameters of a FE model. Shrot and Bäker [17] then used the Levenberg–Marquardt algorithm for their identification of the constitutive material parameters. They showed that similar results (cutting forces and chip morphology) could be obtained by different sets of parameters and therefore highlighted the non-uniqueness of the solution of the inverse problem. In addition to the flow stress parameters, Klocke et al. [18] also identified the damage parameters. In more recent works, such as Bosetti et al. [19] and Denkena et al. [20], the approach to tackle the inverse identification problem is moving from optimization to Artificial Intelligence (AI) based methods. The Downhill Simplex Algorithm (DSA) is adopted by Bergs et al. [21] and by Hardt et al. [22] for AISI 1045. Stampfer et al. [23] also selected the DSA when dealing with AISI 4140 tempered at 3 different temperatures. In [24], Hardt et al. showed that the Particle Swarm Optimization (PSO) was more efficient to solve the inverse problem than the DSA, even if computation time is still significant. In an effort to reduce it, an Efficient Global Optimization (EGO) algorithm has recently been introduced by Kugalur Palanisamy et al. [25]. They simultaneously identified the parameters of the material constitutive model and of the friction model for

Ti6Al4V. Most of these works highlight the non-uniqueness of the identification and they all require the definition of the analytical expression of the constitutive model.

This paper fills the literature gap on oblique cutting by investigating free orthogonal and oblique 3D cutting configurations from both the experimental and the numerical points of view. An Artificial Neural Network (ANN), introduced in Pantalé et al. [26], is implemented in a FE cutting model for the first time instead of the analytical JC law. A broad range of cutting speeds (6), uncut chip thicknesses (3) and cutting edge inclination angles (2) resulting in 36 different conditions is considered to demonstrate the predictive ability of the FE model for fundamental variables. The main goals of a predictive model are the accurate modelling of the trends of the results when the conditions change and the good agreement of the predicted values with the experimental ones (exact values are not looked for due to experimental dispersions). This type of models aims at supporting future choices and developments without the need for experimental data. No assumption is made about the geometry of the machined workpiece in the model (i.e., its width is the same as in the experiments), while keeping computation time relevant for industrial applications. The developments are applied to the formation of continuous chips of titanium alloy Ti6Al4V.

2. Experimental setup

A 3-axis GF Mikron VCE 600 Pro milling machine is used to carry out dry free orthogonal and oblique cutting tests on Ti6Al4V (grade 5 annealed at 750 °C for 1 h followed by air cooling) with the same kinematics as a shaper. As shown in Figure 1, the tungsten carbide tool (modified LCGN160602-0600-FG, CP500 from SECO) is fixed on a dedicated holder (modified CFHN-06 from SECO) and the sample to be cut is clamped in the spindle (no rotation is allowed during the test). The top of the sample includes 3 ribs of 1 mm in width (the width of the tool is 6 mm) and 10 mm in length. The test consists of removing the upper layer (its height is the uncut chip thickness, h) of one rib at the prescribed cutting speed, v_c. The cutting speed is provided by the feed rate, v_f, of the machine (max. value of 40 m/min). The tool cutting edge inclination, λ_s, results from the relative angular orientation of the tool and the sample. Table 1 shows the cutting conditions: 6 cutting speeds, 3 uncut chip thicknesses and 2 inclination angles, each is repeated 3 times.

Forces are measured with a 3-component Kistler 9257B dynamometer and are amplified by a Kistler 5070A charge amplifier. The acquisition is performed at

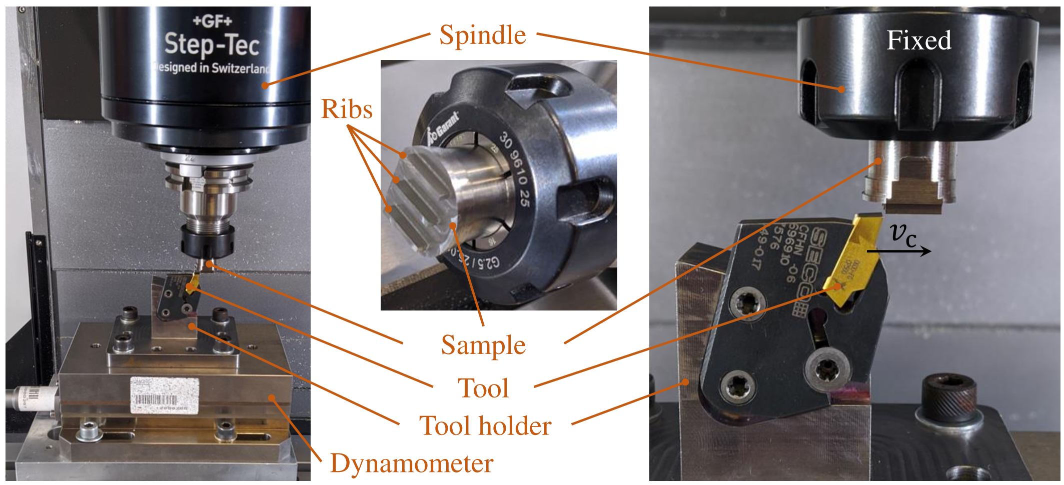

Figure 1: Experimental setup

Table 1: Cutting conditions of the study

Parameter	Values
Cutting speed, v_c (m/min)	5, 7.5, 10, 20, 30, 40
Uncut chip thickness, h (µm)	40, 60, 80
Cutting edge inclination, λ_s (°)	0, 6
Width of the workpiece (mm)	1
Length of the workpiece (mm)	10
Width of the cutting edge (mm)	6 (1.1 in the model)
Cutting edge radius, r_β (µm)	20
Rake angle, γ_0 (°)	15
Clearance angle, α_0 (°)	2

3 kHz with a Kistler 5697A2 data acquisition system and the DynoWare software. Recorded forces are then filtered with a second-order low-pass Bessel filter at 750 Hz before computing the mean value of the signal at the steady state.

All the chips are collected and observed with a Dino Lite digital microscope AM7013MZT (5 MP, magnification 20× – 250×). Each chip is measured 3 times along its length to get a mean value representative of the whole chip.

3. Finite element model

3.1. Modelling choices

The CEL formulation is adopted to model the dry free orthogonal and oblique cutting tests with Abaqus/Explicit 2020. The 3D model is composed of a fixed Lagrangian tool and a Eulerian workpiece (Figure 2). Chip formation occurs by plastic flow across the Eulerian domain with no mesh distortion. The Eulerian formulation enables to form chips without damage properties, removing modelling assumptions. These two characteristics contribute to cutting models providing accurate results and realistic chips [8].

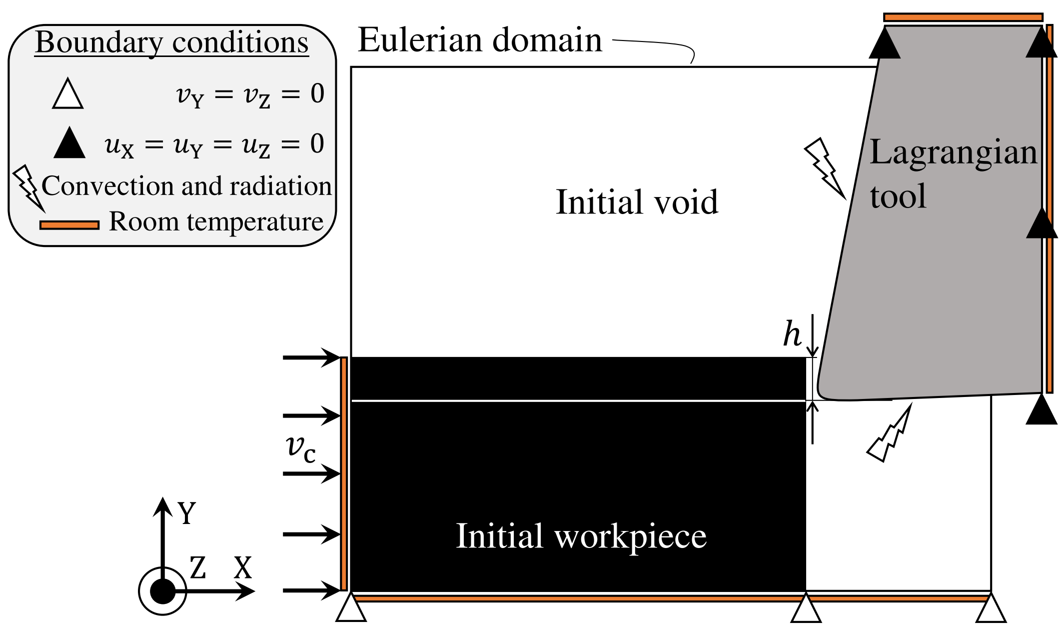

Figure 2: Boundary conditions and schematic initial geometry of the model

As shown in Figure 3, the full width of the workpiece (1 mm), i.e., a rib in the experiments, is modelled. To allow chip formation and side flow, the Eulerian domain is wider (it includes the volume in which material can move). The volume above the initial workpiece is also meshed with Eulerian elements for the same reasons. As in the experiments and to fulfil the hypothesis of free orthogonal and oblique cutting, the tool is wider than the workpiece (it is 1.1 mm in the model and 6 mm in the experiments). It is very important to stress that the models are the same for both inclination angles: they only differ by the rotation of the tool of 6° about Y axis as in the experiments (Figure 3). This, coupled with the absence of assumptions when developing the models, contributes to make the models predictive: no input is changed when cutting conditions do.

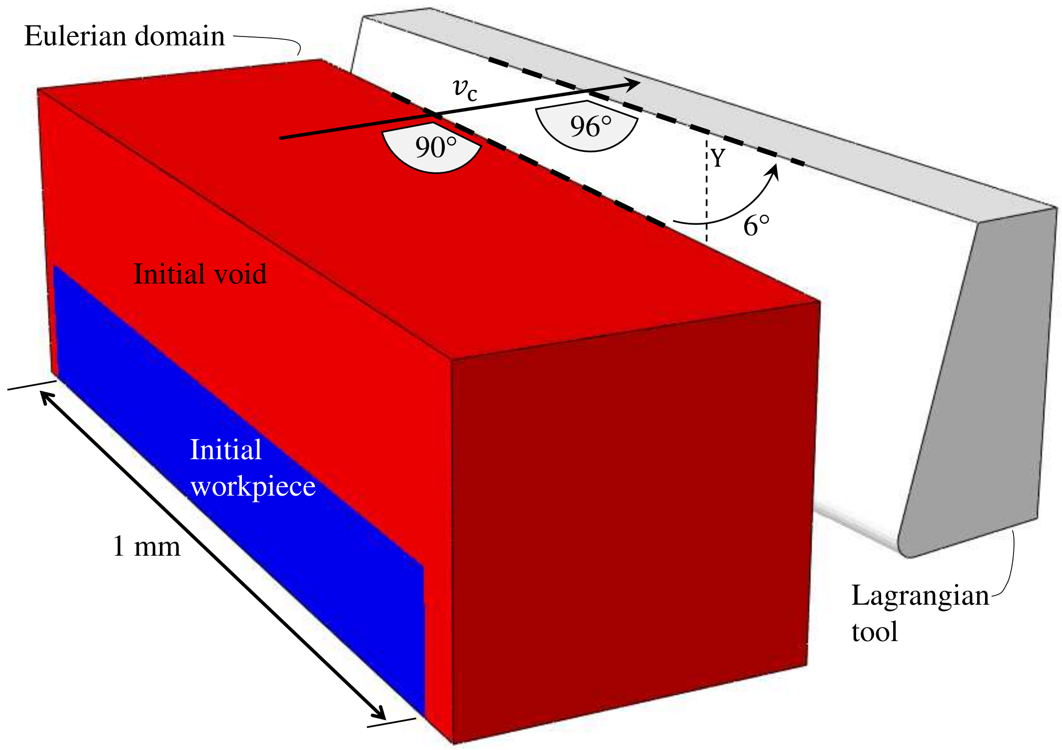

Figure 3: Configuration of the FE model for $\lambda_s = 6°$

According to a previous mesh sensitivity study in orthogonal cutting with the CEL formulation [9], elements edge size is 5 µm in the plane parallel to the cutting speed. In the direction perpendicular to this plane, it is 5 µm in areas close to the lateral boundaries of the Eulerian domain and 50 µm in the middle of the workpiece. To reduce computation time, the size of the model depends on the value of the uncut chip thickness. This results in a Eulerian domain (EC3D8RT linear 3D Eulerian elements with 8 nodes, coupled mechanical-thermal behaviour and reduced integration) composed of 216 550 to 273 350 nodes and a Lagrangian domain (C3D8T linear 3D Lagrangian elements with 8 nodes, coupled mechanical-thermal behaviour) of 4650 nodes.

The Ti6Al4V workpiece is assumed to be thermo-elasto-viscoplastic (isotropic) and the inelastic heat fraction is 0.9. JC set of parameters from Seo et al. [27] is adopted as the value of A corresponds to the typical yield stress value of Ti6Al4V and this set proved to provide the best results among 20 sets available in the literature [28]. The tungsten carbide tool with TiN coating is assumed to be linear elastic. Material properties are provided in Table 2.

Table 2: Materials properties [27, 29, 30]

Young's modulus, E (GPa)	Ti6Al4V	113.8*
	WC	650
Poisson's ratio, ν	Ti6Al4V	0.34
	WC	0.2
Density, ρ (kg/m^3)	Ti6Al4V	4430
	WC	14 850
Conductivity, k (W/m K)	Ti6Al4V	6.3*
	WC	100
Expansion, α (1/K)	Ti6Al4V	8.6E−6*
	WC	5E−6
Specific heat, c_p (J/kg K)	Ti6Al4V	531*
	WC	202
JC constitutive model	A (MPa)	997.9
	B (MPa)	653.1
	C	0.0198
	m	0.7
	n	0.45
	$\dot{\varepsilon}_0$ (1/s)	1
	T_{room} (K)	293
	T_{melt} (K)	1873

*: Dependence on the temperature, value provided at 293 K

Following the experimental results of Rech et al. [31], Coulomb's friction is assumed to occur at the tool-workpiece interface and both friction, μ, and heat partition, β, coefficients depend on the cutting speed. Limiting shear stress, $\tau_{\max}$, is included and is given by

$$\tau_{\max} = \frac{\text{yield stress}}{\sqrt{3}} = \frac{A}{\sqrt{3}} \tag{2}$$

All the friction energy is converted into heat. Table 3 shows the friction coefficients adopted in this study.

Table 3: Friction and heat transfer coefficients [29, 31]

Cutting speed, v_c (m/min)	μ	β
5	0.24	1
7.5	0.22	0.89
10	0.21	0.80
20	0.19	0.63
30	0.18	0.55
40	0.17	0.50
Limiting shear stress, $\tau_{\max}$ (MPa)	576	
Convection, U (W/m^2 K)	50	
Radiation, ϵ	0.3	

A room temperature of 293 K is imposed on the upper and right surfaces of the tool and on the left and bottom surfaces of the workpiece (Figure 2). Radiation and convection are assumed to occur on the rake and clearance faces of the tool. The initial temperature of the tool and the workpiece is set to room temperature (293 K). Heat transfer coefficients are provided in Table 3.

3.2. Material constitutive model of Ti6Al4V

The constitutive model of the Ti6Al4V material used in all the numerical simulations proposed in section 4 is a thermo-elasto-viscoplastic law using a flow criterion based on an ANN identified for the selected material and implemented in the Abaqus/Explicit code via a Fortran routine VUHARD as proposed by Pantalé et al. in [26]. The principle of this approach consists in replacing the analytical formulation of the flow law, based on a Johnson-Cook or Zerilli-Armstrong type model, and allowing the calculation of the flow stress σ^y as a function of the plastic strain ε^p, of the plastic strain rate, $\dot{\varepsilon}^p$, and of the temperature T, by a multi-layer ANN serving as a universal approximator. Thus, the parameters of the neural network can directly be identified from the experimental data without having to postulate a behavioural model, which simplifies the procedure and allows more flexibility in the definition of the model. The proposed approach also allows, as shown in Pantalé et al. [26], to compute the derivatives of the flow stress σ^y with respect to the three input variables of the model, a necessary step to implement this model as a flow law in the form of a VUHARD subroutine in the Abaqus/Explicit FEM code.

In order to verify the influence of the complexity of the neural network on the numerical results of the simulation and on the computing time, several architectures of ANN are tested thereafter (in 3.4). The chosen global architecture has 2 hidden layers with a variable number of neurons for the first hidden layer (ζ = 9 to 17) and 7 neurons for the second hidden layer, 3 inputs (plastic strain, ε^p, plastic strain rate, $\dot{\varepsilon}^p$, and temperature, T) and one output (the yield stress, σ^y). The global architecture of this kind of ANN is given in Figure 4 for 9 neurons in the first hidden layer. Conforming to Pantalé et al. [26], this ANN is referred to after the terminology ANN 3-9-7-1-sig, because it has 3 inputs, 9 neurons in the first hidden layer, 7 neurons in the second hidden layer, 1 output and a sigmoid activation function.

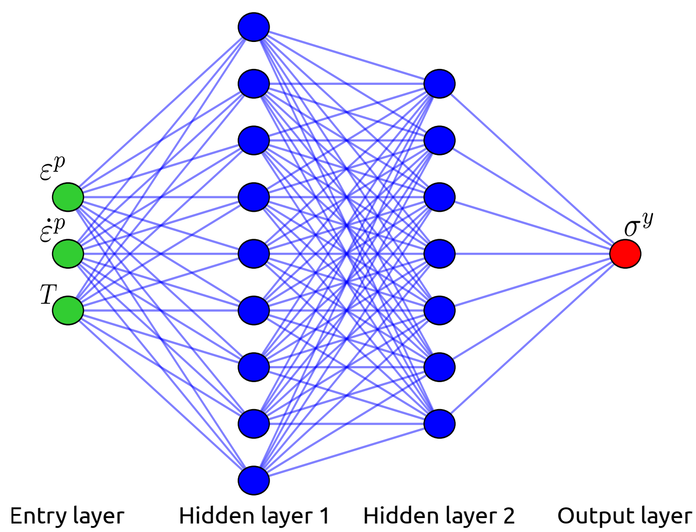

Figure 4: Architecture of the ANN 3-9-7-1-sig used for the flow law

The main advantage of this approach (the use of an ANN), after the training phase, is that the output σ^y of the network is related to the inputs ε^p, $\dot{\varepsilon}^p$, and T through equations (3) to (7). The first step is to scale the input data to the interval $[0, 1]$ using the following equation:

$$\overrightarrow{x} = \begin{cases} x_1 = \frac{\varepsilon^p - [\varepsilon^p]_{min}}{[\varepsilon^p]_{max} - [\varepsilon^p]_{min}} \\ x_2 = \frac{\ln(\dot{\varepsilon}^p) - [\ln(\dot{\varepsilon}^p)]_{min}}{[\ln(\dot{\varepsilon}^p)]_{max} - [\ln(\dot{\varepsilon}^p)]_{min}} \\ x_3 = \frac{T - [T]_{min}}{[T]_{max} - [T]_{min}} \end{cases} \quad (3)$$

The outputs of the neurons in the first hidden layer are given by the following equation:

$$\overrightarrow{y_1} = \text{sig}\left(\mathsf{W}_1 \cdot \overrightarrow{x} + \overrightarrow{b_1}\right) \tag{4}$$

where, sig() is the sigmoid activation function defined by equation (5):

$$\text{sig}(x) = \frac{1}{1 + \mathrm{e}^{-x}} \tag{5}$$

Then, the output of the neurons in the second hidden layer are given by equation (6):

$$\overrightarrow{y_2} = \text{sig}\left(\mathsf{W}_2 \cdot \overrightarrow{y_1} + \overrightarrow{b_2}\right) \tag{6}$$

So, the output of the ANN is therefore given by equation (7).

$$\sigma^y = ([\sigma^y]_{max} - [\sigma^y]_{min})\left(\overrightarrow{w}^T \cdot \overrightarrow{y_2} + b\right) + [\sigma^y]_{min} \tag{7}$$

In equations (3) to (7), quantities W_1, W_2, $\overrightarrow{w}$, $\overrightarrow{b_1}$, $\overrightarrow{b_2}$ and b are given by the training procedure of the ANN. Corresponding values for an ANN containing 9 neurons in the first hidden layer are reported in Appendix A. Quantities $[\ ]_{min}$ and $[\ ]_{max}$ are the boundaries of the range of the corresponding field during the training phase, values are also given in Appendix A.

Because of the large number of identified parameters for all the ANN models (from 114 to 202 for 9 and 17 neurons for the first hidden layer, respectively), the other 4 sets of ANN parameters used in this publication can be found in [32]. [FD:] Inclure dans corps du texte puisque article normal et rq reviewer?

3.3. Sensitivity study of the results to mass scaling

FE modelling of the cutting process is very expensive in CPU computation time because of the coupling of many nonlinear phenomena and the large amount of tiny finite elements. Mass scaling (MS) is introduced in the model to reduce the CPU computation time while checking that it does not influence the results (forces and energies) via a mass scaling sensitivity study. MS factors, MS_f, ranging from 1E6 (theoretical scaling of CPU time of $\sqrt{MS_f} = 1000$) to 1 (no scaling) have been used for one cutting condition ($\lambda_s = 0°$, $v_c = 30\,\text{m/min}$ and $h = 60\,\mu\text{m}$). The same signal processing procedure is applied to the numerical forces as to the experimental forces (cf. 2): they are filtered with a second-order low-pass Bessel filter at 750 Hz before computing the mean value at steady state. Table 4 gives the results of the model with MS normalized ($\hat{F}_i$) by these of the model without MS:

$$\hat{F}_i = \frac{F_i \text{ with MS}}{F_i \text{ without MS}} \tag{8}$$

with $i = c$ for the cutting force and $i = f$ for the feed force. As expected, actual speed-up does not increase linearly with the MS_f, but it is still significant. MS_f of 1E6 leads to unstable computation and MS_f of 1E5 results in erratic forces evolutions. These results are confirmed by high values of the kinetic (KE) on internal (IE) energies ratio (it should not exceed a few % [33, 34]). An MS_f value of 1E3 is selected as it provides a good balance between computation time reduction and impact on forces, while keeping $\frac{KE}{IE}$ below 1%. To provide an order of magnitude of CPU computation time, between 10 h and 50 h (depending on the value of h) are needed on 4 cores of an Intel i7-5700HQ CPU at 2.7–3.5 GHz.

Table 4: MS sensitivity study (selected MS factor, MS_f, in bold, $\hat{F}_c$: normalized cutting force, $\hat{F}_f$: normalized feed force, KE: kinetic energy, IE: internal energy)

MS_f	CPU scaling	Speed-up	$\hat{F}_c$	$\hat{F}_f$	$\frac{KE}{IE}$ (%)
1	1	1	1	1	2.3E−4
1E2	10	9	1.006	0.982	2.2E−2
1E3	**32**	**21**	**1.008**	**0.940**	**2.2E−1**
1E4	100	61	1.012	0.921	2.4
1E5	316	173	Erratic	Erratic	22
1E6	1000	207	Unstable	Unstable	58

3.4. Sensitivity study of the results to the number of neurons

The number of neurons on the hidden layers may influence the results. A sensitivity study on the number of neurons for the first hidden layer, ζ, is carried out to select the ANN providing the best balance between CPU computation time and quality of the results. The results of the study are provided in Table 5. $\check{F}_i$ corresponds to the results of the model with ANN normalized by these of the model with the built-in JC model:

$$\check{F}_i = \frac{F_i \text{ with ANN}}{F_i \text{ with JC}} \tag{9}$$

They show no influence on the forces when compared to the built-in Johnson-Cook model, only computation time is influenced. A first hidden layer with 9 neurons is therefore selected as it leads to the lowest CPU computation time increase.

Table 5: Sensitivity of the forces to the number of neurons of the first layer, ζ (selection in bold, $\check{F}_c$: normalized cutting force, $\check{F}_f$: normalized feed force)

ζ	Time increase (%)	$\check{F}_c$	$\check{F}_f$
Built-in	0	1.000	1.000
9	**6**	**1.000**	**0.999**
11	6	1.001	1.000
13	7	1.000	0.998
15	8	1.001	1.001
17	10	1.000	1.000

4. Experimental and numerical results

An example of temporal evolutions of numerical and experimental forces is plotted for the 3 directions in Figure 5 at $\lambda_s = 6°$, $v_c = 10\,\mathrm{m/min}$ and $h = 40\,\mathrm{m/min}$. Computation of the FE models is carried out until a few microseconds after the steady state is reached. Then, linear extrapolation (dashed line between the two last markers in Figure 5) is used to provide numerical values during the same time range as the experimental values. Mean and standard deviation ($2\,\sigma$) are computed from the 3 experimental values. The resulting dispersion is plotted in Figure 5 around the mean values of each force. Steady state takes more time to be reached for the experiments than in the numerical model, particularly for the cutting force. Dispersion around the mean force evolution is larger for the feed force than for the cutting force, while the mean feed force value is 46% of the mean cutting force value. The numerical cutting force is very close to the experimental mean cutting force; it is only 4% larger. This difference, Δj, is computed by

$$\Delta j = \frac{\left| j^{(\mathrm{sim})} - j^{(\mathrm{exp})} \right|}{j^{(\mathrm{exp})}} \times 100 \tag{10}$$

with j the cutting force, the feed force, the passive force or the chip thickness. $j^{(\mathrm{sim})}$ is the mean value from the simulation, while $j^{(\mathrm{exp})}$ is the mean experimental value.

The numerical feed force is underestimated by the model, but it is at the boundary of the 95% experimental confidence interval. The numerical passive force difference is also underestimated and it is not in the narrower experimental dispersion. The difference between the mean values of experimental and numerical feed and passive forces is 25%. A feed force less well modelled than the cutting force is typical of FE models of the cutting process and the difference with the experimental value is similar to other studies for a less extensive range of cutting conditions [7, 35–38]. Hardt and Bergs [12] also obtained higher differences for the feed and the passive force than for the cutting force. The difference for the passive force was higher than for the feed force, which is the opposite observation from this work.

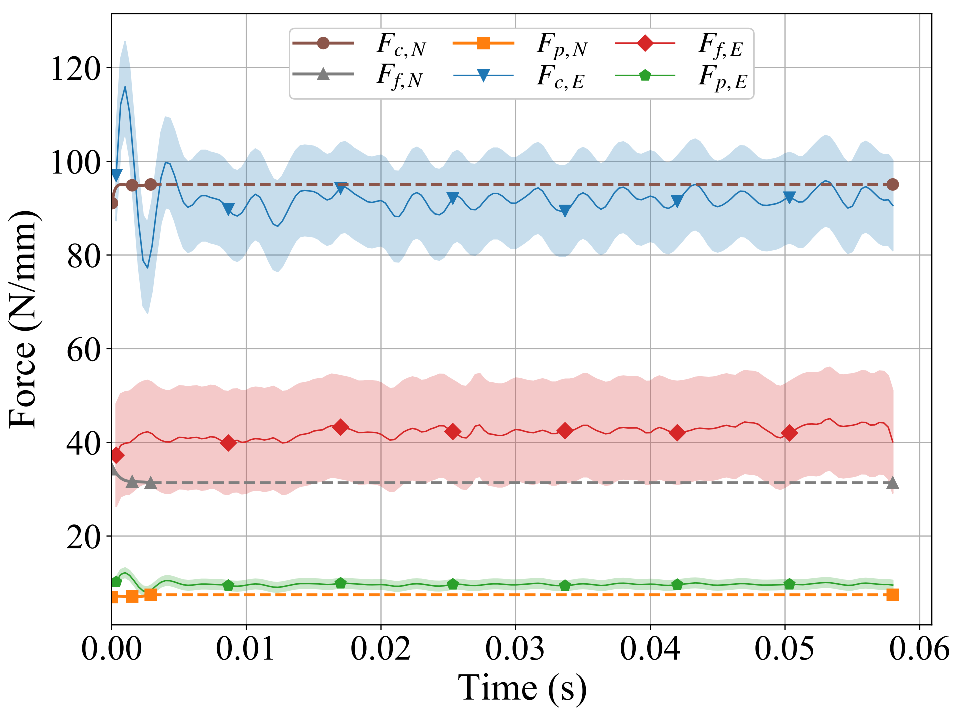

Figure 5: Temporal evolutions of experimental (E) and numerical (N) forces at $\lambda_s = 6°$, $v_c = 10\,\mathrm{m/min}$ and $h = 40\,\mu\mathrm{m}$ with dispersion around mean experimental values (linear extrapolation of numerical values in dashed)

Numerical chips at $v_c = 10\,\mathrm{m/min}$ and $h = 40\,\mu\mathrm{m}$ for $\lambda_s = 0°$ and $\lambda_s = 6°$ are provided in Figures 6 and 7. When the cutting edge inclination is 0°, both sides of the chip are identical and a symmetry plane can be drawn in the middle of the workpiece (Figure 7 (a)). On the contrary, for the cutting edge inclination of 6°, the chip is not aligned with the workpiece any more. The chip bends on one side due to the orientation of the tool and the symmetry is lost for both the geometry, and the thermal and mechanical fields as highlighted in Figure 7 (b). This produces helical chips for the inclination angle of 6° as in the experiments. Figure 8 shows the variation of the chip thickness across its width: it is thicker in the middle (i.e., the body of the chip) than on its sides. This stresses the importance of 3D modelling, even for the orthogonal cutting configuration as previously highlighted [9]. 3D modelling also allows to reproduce the side flow occurring in the experiments for both cutting edge inclination values (Figure 6), contrary to a 2D model [3, 9, 10]. Although this leads to higher computation times, future cutting models should be in 3D, even when orthogonal cutting is considered. In this case, it is recommended to take advantage of the symmetry of the configuration to reduce computation time. This simplification has not been included in this study to avoid any difference in the FE models between the 2 cutting edge inclinations.

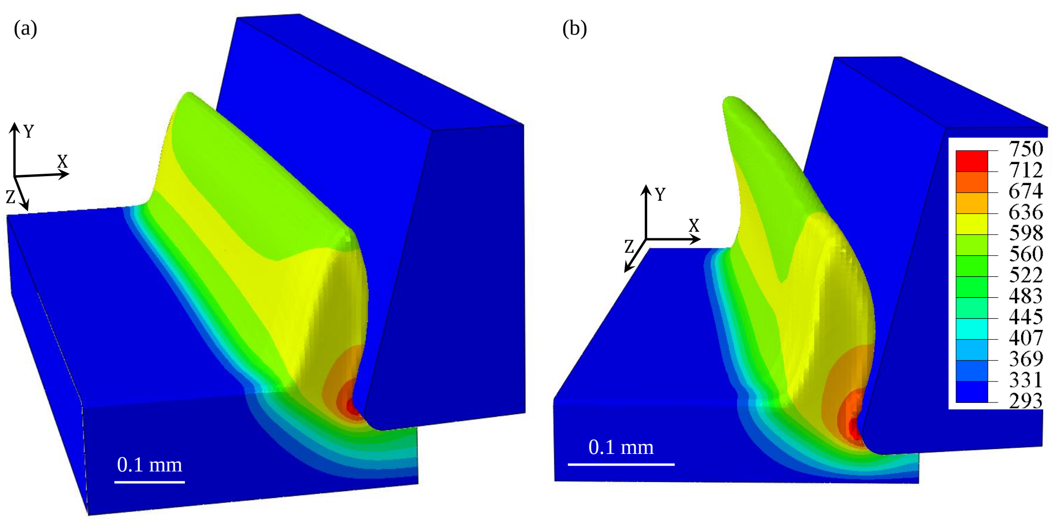

Figure 6: Temperature contours (in K) of the numerical chip after 1.5 ms at $v_c = 10\,\mathrm{m/min}$, $h = 40\,\mu\mathrm{m}$ and (a) $\lambda_s = 0°$, (b) $\lambda_s = 6°$

Mean values of the experimental forces and their dispersion are shown in Figures 9 to 13 together with the mean numerical values. Passive force values are of

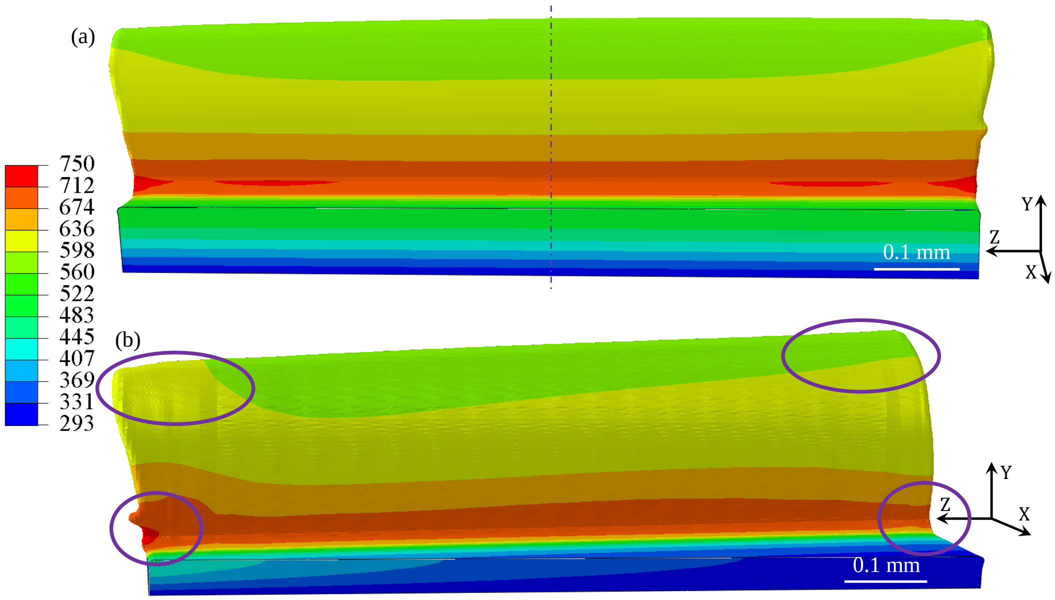

Figure 7: Temperature contours (in K) of the back of the numerical chip (tool is removed) after 1.5 ms at v_c = 10 m/min, h = 40 µm and (a) $\lambda_s = 0°$, (b) $\lambda_s = 6°$

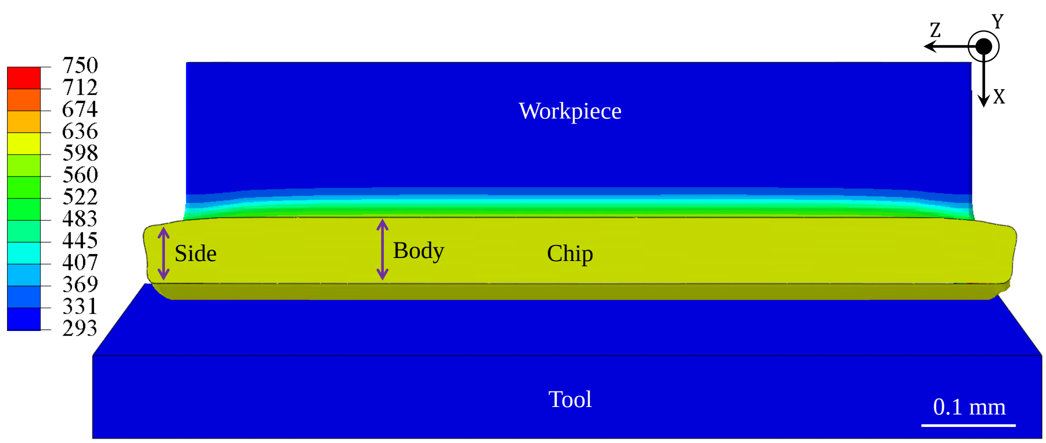

Figure 8: Temperature contours (in K) of the top of the numerical chip after 1.5 ms at v_c = 10 m/min, h = 40 µm and $\lambda_s = 0°$

course only plotted for $\lambda_s = 6°$ as they are equal to zero when $\lambda_s = 0°$.

The increase of the cutting force with the uncut chip thickness is clearly observed in Figures 9 and 10 for both experimental and numerical results at the 2

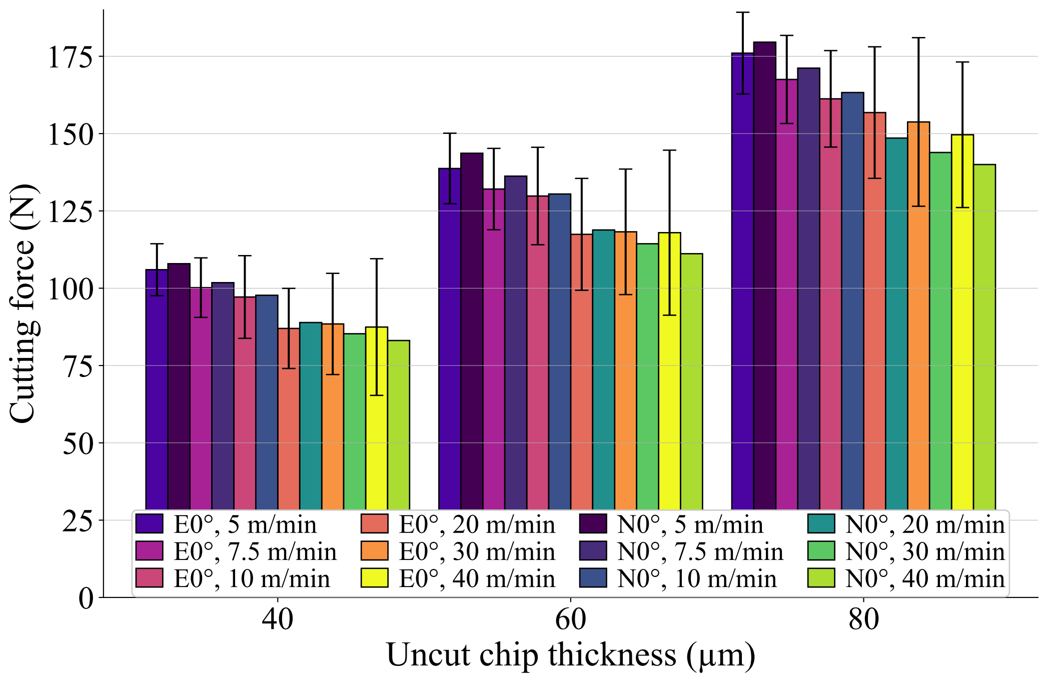

Figure 9: Comparison of experimental (E) and numerical (N) cutting forces at the cutting edge inclination of 0° for the 3 uncut chip thicknesses (40, 60 and 40 µm) and the 6 cutting speeds (5, 7.5, 10, 20, 30 and 40 m/min)

inclination angles, as well as the decrease of the force with the increase in the cutting speed. This shows temperature softening domination on strain rate hardening for Ti6Al4V and that it is accurately modelled. The increase of the inclination angle from 0° to 6° slightly reduces the cutting force; this is well captured by the model. For cutting speeds of 20–40 m/min and inclination angle of 0°, F_c is almost constant with the cutting speed for uncut chip thicknesses of 40 µm and 60 µm, while it slightly decreases for 80 µm; this small stabilization is less marked for the modelling.

An increase in the deviation around the mean value with the cutting speed is noted for values above 10 m/min. All numerical values are within a confidence interval of 95% of the experiments (35 out of 36 conditions are within a confidence interval of 68%). The mean difference with the experiments is 4%, which is remarkable, moreover given the wide range of cutting conditions considered and the absence of tuning of the model. This highlights the predictive ability and the accuracy of the FE model for both inclination angles.

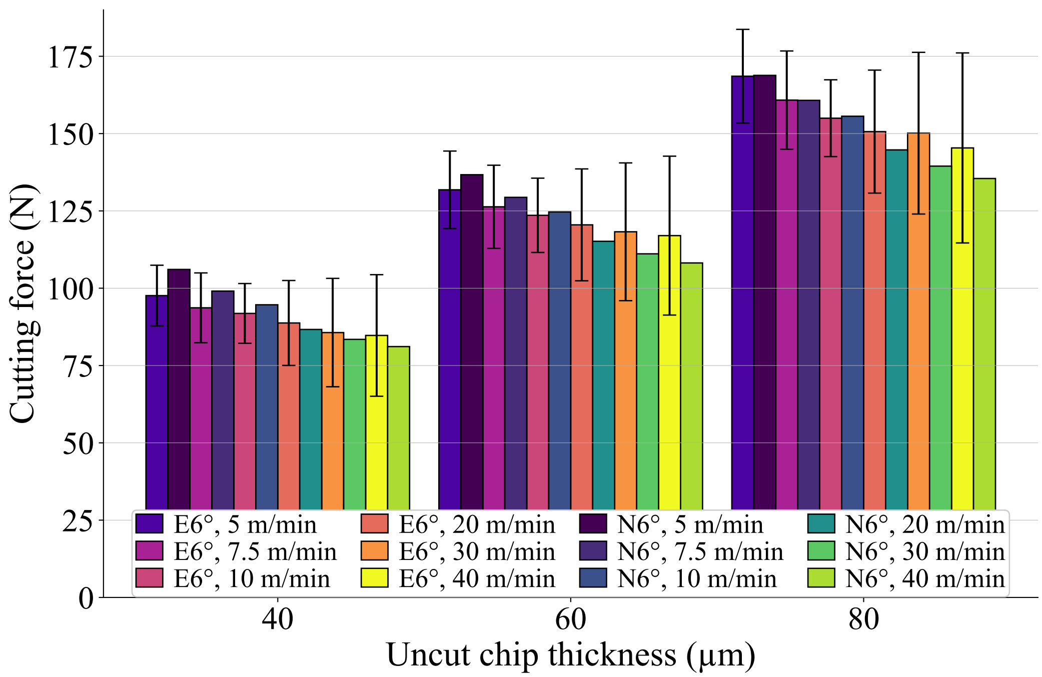

Figure 10: Comparison of experimental (E) and numerical (N) cutting forces at the cutting edge inclination of 6° for the 3 uncut chip thicknesses (40, 60 and 80 µm) and the 6 cutting speeds (5, 7.5, 10, 20, 30 and 40 m/min)

Figures 11 and 12 show the results for the feed force, where the two clearest trends for the experiments are its decrease with inclination angle and its increase with the uncut chip thickness (even if it is smaller than the expectations). For 80 µm, F_f globally decreases with v_c in the experiments. For 40 µm and 60 µm, the force decreases at lower v_c and then increases for 0°, while a decrease is observed at all v_c for 6° (experimental dispersion is high for both inclination angles, but the mean trend with the cutting speed is clear at 6°, not at 0°). For the numerical values, the global trend is the same for the 3 uncut chip thicknesses and both inclination angles: a decrease for the lowest v_c values and then an increase. It must be noted that the numerical model does not handle correctly the feed force trends: as clearly shown by Figure 12, the numerical forces have globally an increasing trend with the cutting speed, while their mean value mostly decreases when the uncut chip thickness increases. Differences between the mean numerical and experimental values increase with the uncut chip thickness: forces are closer at 40 µm than at 80 µm. The numerical values are mostly not within the 95% confi-

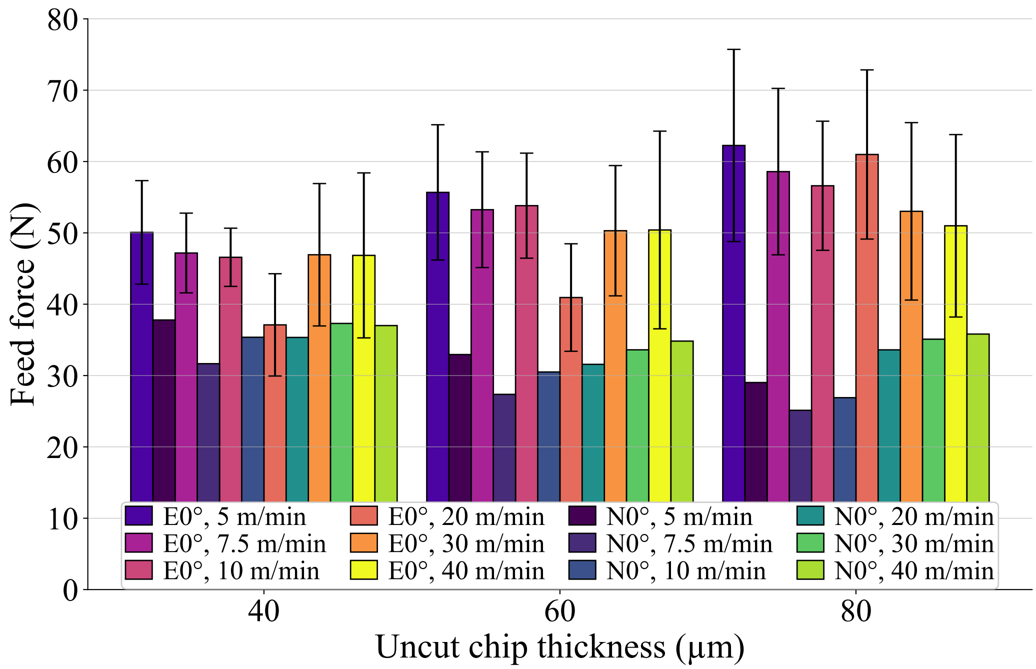

Figure 11: Comparison of experimental (E) and numerical (N) feed forces at the cutting edge inclination of 0° for the 3 uncut chip thicknesses (40, 60 and 80 μm) and the 6 cutting speeds (5, 7.5, 10, 20, 30 and 40 m/min)

dence interval (it has no clear evolution with the cutting conditions). Coupled with the differences in trends, it shows that F_f is less well modelled (mean difference is 39%) than F_c as usual in FE modelling of the cutting process and even more so in 3D [12]. The influence of the uncut chip thickness on the feed force should therefore be improved. Material constitutive model parameters are known to have an impact on the forces (and on the chip morphology) [25, 28]. The friction model should be improved as well to enhance the results [12].

Passive force is non-zero for the inclination angle of 6° (Figure 13). As the cutting force, it increases with the uncut chip thickness and it decreases with the cutting speed. Comparison with the experiments is globally the same as for F_c, except for a larger difference in the magnitude of F_p (mean difference is 26%, but it is small in absolute – less than 5 N). The numerical values are mostly not in the 95% experimental confidence interval. A lower magnitude of the passive force from the simulation than from the experiments with the right trends when the cutting conditions changed was also observed by Hardt and Bergs [12]. Differences

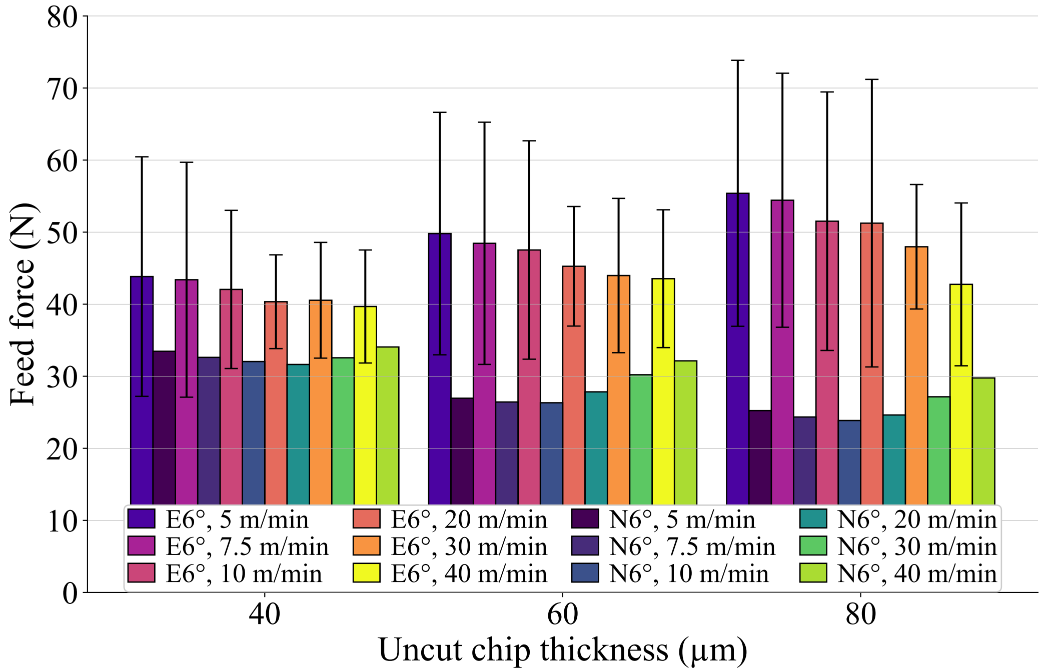

Figure 12: Comparison of experimental (E) and numerical (N) feed forces at the cutting edge inclination of 6° for the 3 uncut chip thicknesses (40, 60 and 80 μm) and the 6 cutting speeds (5, 7.5, 10, 20, 30 and 40 m/min)

were mainly attributed to differences in the cutting edge radius, the modelling of friction and the material constitutive model. In this work, impact of the cutting edge radius can be neglected as it is the same in the model as in the experiments.

Regarding the chips morphology, all the chips are continuous. For both the simulation and the experiments, the chip thickness ratio, λ_h:

$$\lambda_h = \frac{h'}{h} \tag{11}$$

with h the uncut chip thickness and h' the chip thickness, is almost independent of the uncut chip thickness (Figures 14 and 15). It is slightly reduced from $\lambda_s = 0°$ to $\lambda_s = 6°$, meaning that the chip thickness decreases with the inclination angle. This influence is underestimated by the model: the reduction of λ_h is lower than in the experiments. The mean difference between experimental and numerical λ_h is 17% across the whole range of cutting conditions. The chip thickness ratio decreases with the cutting speed because of the reduction of friction, which is correctly

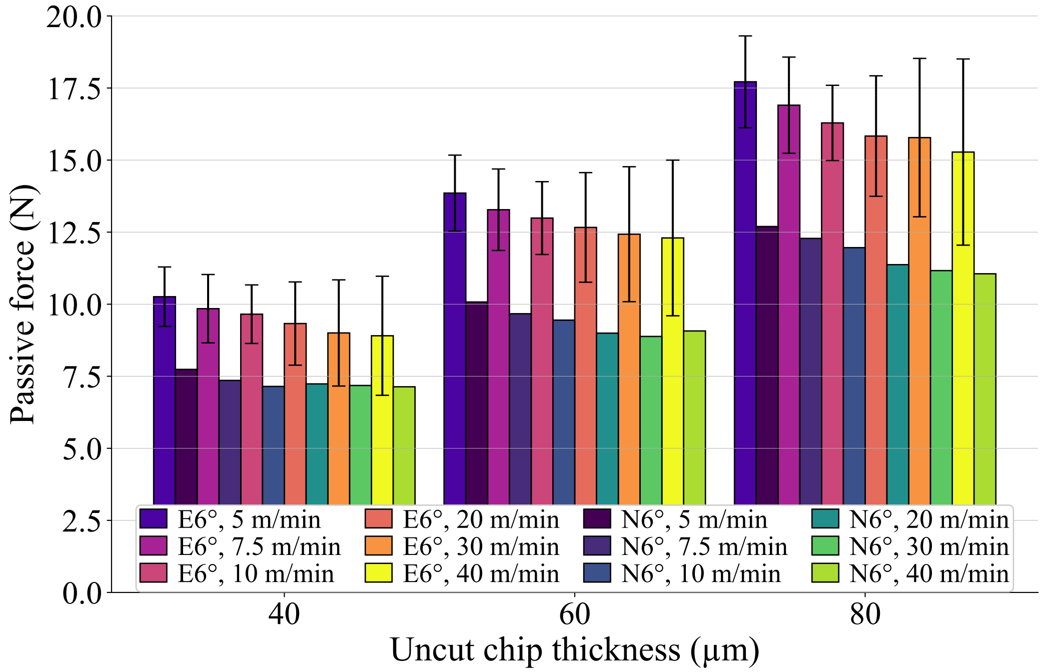

Figure 13: Comparison of experimental (E) and numerical (N) passive forces at the cutting edge inclination of 6° for the 3 uncut chip thicknesses (40, 60 and 80 µm) and the 6 cutting speeds (5, 7.5, 10, 20, 30 and 40 m/min)

captured by the model. As for the feed force, the results should be improved by more complex friction models and a set of material constitutive parameters for which the identification includes the forces and the chip thickness [25].

Differences computed according to equation 10 are shown in Table 6 to provide a quantitative overview of the results. The cutting force is the best modelled quantity as observed in the literature. This results could be expected as the set of parameters of the constitutive model was selected mainly thanks to its good approximation of the cutting force [28]. As that selection was carried out with a 2D model, the results show the capacity of the model to correctly handle the third (passive) force. Based on the mean differences, the performance of the model is very close for the cutting and the feed forces for both cutting edge inclinations, even if a small degradation (1% and 2%, respectively) is noted for 6°. This degradation is larger (7%) for the chip thickness ratio and should be linked with the difference in the passive force. Indeed, the modellings of the chip thickness and of the out-of-plane force are deeply linked. Improving the friction at the tool –

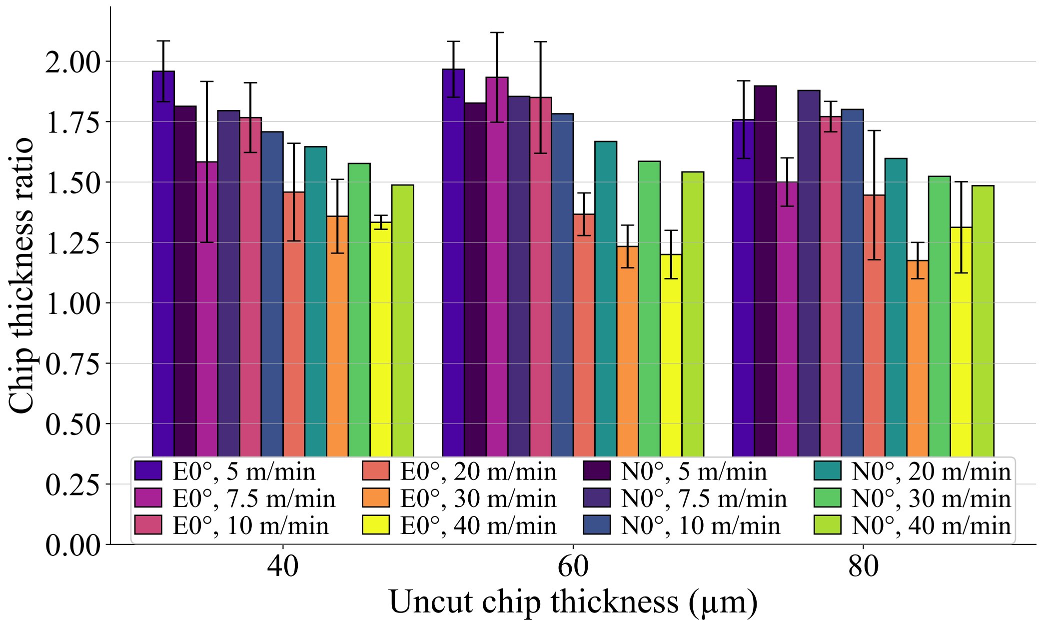

Figure 14: Comparison of experimental (E) and numerical (N) chip thickness ratios at the cutting edge inclination of 0° for the 3 uncut chip thicknesses (40, 60 and 80 µm) and the 6 cutting speeds (5, 7.5, 10, 20, 30 and 40 m/min)

workpiece interface should be a key point. It must be noted that the chip thickness is very well modelled in some cutting conditions with a minimal difference of 2 %. The difference is larger for the feed force than for the passive force, an opposite trend to Hardt and Bergs' [12]. Both mean and range (min – max) of differences are larger for the feed force. The smaller range of the passive force confirms an offset for all the cutting conditions, similarly to the results of Hardt and Bergs [12]. Again, the modelling of friction should be the first aspect of the model to improve in future developments.

5. Conclusions

An experimental and numerical study of the free orthogonal and oblique cutting of Ti6Al4V has been carried out for a wide range of cutting conditions using an ANN-based material constitutive model. The following main conclusions are drawn:

- The experimental study has been carried out with the same setup in free or-

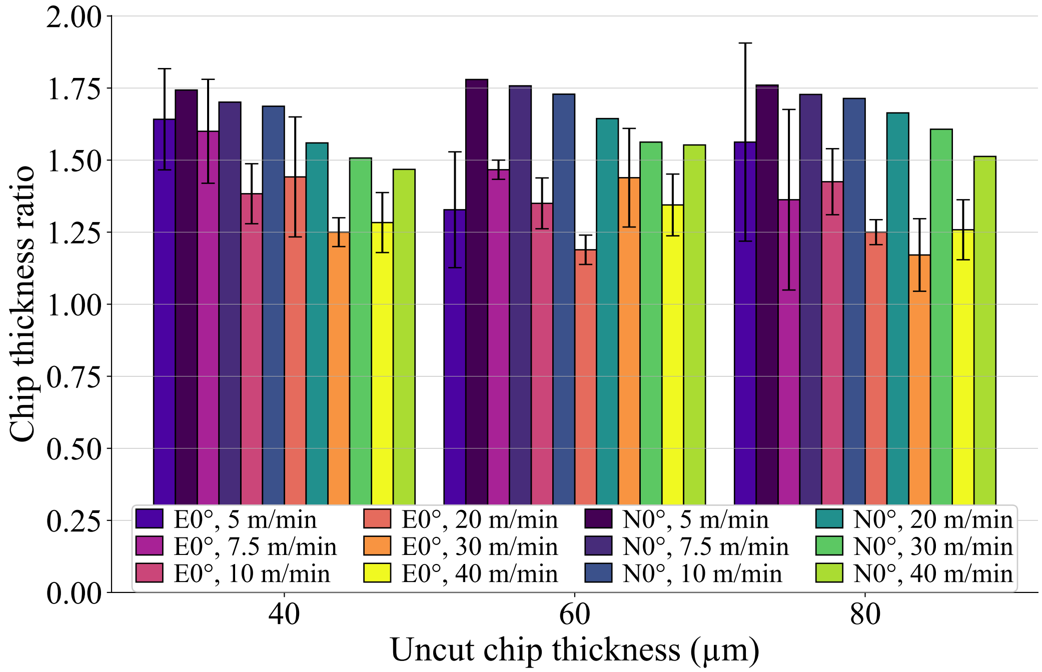

Figure 15: Comparison of experimental (E) and numerical (N) chip thickness ratios at the cutting edge inclination of 6° for the 3 uncut chip thicknesses (40, 60 and 80 µm) and the 6 cutting speeds (5, 7.5, 10, 20, 30 and 40 m/min)

Table 6: Synthetic quantitative overview of the results: differences between the experimental and the numerical results (mean difference for each cutting edge inclination, and maximal, minimal and mean differences for all the conditions) for the cutting force, ΔF_c, the feed force, ΔF_f, the passive force, ΔF_p, and the chip thickness ratio, $\Delta \lambda_h$

Difference	ΔF_c (%)	ΔF_f (%)	ΔF_p (%)	$\Delta \lambda_h$ (%)
Mean $\lambda_s = 0°$	3	38	–	14
Mean $\lambda_s = 6°$	4	40	26	21
Max global	10	60	29	38
Min global	1	10	19	2
Mean global	4	39	26	17

thogonal and free oblique cutting for the titanium alloy Ti6Al4V (the only change is the cutting edge inclination). It is a reference to assess the performances of the 3D FE model introducing an ANN-based constitutive model and developed in the same conditions. An unpreviously seen wide range of cutting conditions, 36, is considered, including 2 cutting edge inclinations.

- Accurate evaluation of fundamental variables and their trends in 3D with the absence of tuning of both numerical parameters and model features when cutting conditions and inclination angle are significantly modified is a strong novelty of this work. Only changing the inclination angle to move from free orthogonal to oblique cutting while maintaining the quality of the results has no equivalent in the current literature, moreover as no study (experimental or numerical) on free oblique cutting is available.

- [FD:] Add one bullet on ANN and the associated future works?

- The cutting force is the best modelled quantity with a mean difference of 4 % with the experiments. The chip thickness ratio and the passive force show a higher deviation with the experiments (17% and 26%, respectively), while their trends when the cutting conditions change are accurate. This corresponds to the expected results provided by a predictive model. The difference for the feed force is higher (39%), and opposite trends by comparison with the experimental reference are observed. The absence of influence of the uncut chip thickness on friction in the model seems to be one of the aspects to include first in future works. The model turns out to handle the apparition of the third, out-of-plane, force well with no significant degradation of the results.

- Predictive abilities of the model make it adequate for the development of tools with a straight cutting edge, for example. This work moreover demonstrates the ability to model materials' behaviour with ANN and opens possibilities in this promising direction.

References

[1] P. J. Arrazola, T. Özel, D. Umbrello, M. Davies, I. S. Jawahir, Recent advances in modelling of metal machining processes, CIRP Annals 62 (2013) 695–718.

[2] M. Agmell, V. Bushlya, S. V. A. Laakso, A. Ahadi, J.-E. Ståhl, Development of a simulation model to study tool loads in pcBN when machining AISI 316L, Int J Adv Manuf Technol 96 (2018) 2853–2865.

[3] X. Xu, J. Outeiro, J. Zhang, B. Li, W. Zhao, Simulation of material side flow using a 3D coupled Eulerian-Lagrangian approach and a constitutive model considering the stress state, Procedia CIRP 102 (2021) 441–446.

[4] M. Abouridouane, T. Bergs, D. Schraknepper, G. Wirtz, Friction behavior in metal cutting: Modeling and simulation, Procedia CIRP 102 (2021) 405–410.

[5] F. Ducobu, E. Rivière-Lorphèvre, E. Filippi, Experimental contribution to the study of the Ti6Al4V chip formation in orthogonal cutting on a milling machine, Int J Mater Form 8 (2015) 455–468.

[6] A. Sela, G. Ortiz-de-Zarate, D. Soler, G. Germain, P. Aristimuño, P. J. Arrazola, Measurement of plastic strain and plastic strain rate during orthogonal cutting for Ti-6Al-4V, International Journal of Mechanical Sciences 198 (2021) 106397.

[7] M. Afrasiabi, J. Saelzer, S. Berger, I. Iovkov, H. Klippel, M. Röthlin, A. Zabel, D. Biermann, K. Wegener, A Numerical-Experimental Study on Orthogonal Cutting of AISI 1045 Steel and Ti6Al4V Alloy: SPH and FEM Modeling with Newly Identified Friction Coefficients, Metals 11 (2021) 1683.

[8] F. Ducobu, E. Rivière-Lorphèvre, E. Filippi, Application of the Coupled Eulerian-Lagrangian (CEL) method to the modeling of orthogonal cutting, Eur J Mech A Solids 59 (2016) 58–66.

[9] F. Ducobu, E. Rivière-Lorphèvre, E. Filippi, Finite element modelling of 3D orthogonal cutting experimental tests with the Coupled Eulerian-Lagrangian (CEL) formulation, Finite Elements in Analysis and Design 134 (2017) 27–40.

[10] D. Ambrosio, A. Tongne, V. Wagner, G. Dessein, O. Cahuc, A new damage evolution criterion for the coupled Eulerian-Lagrangian approach: Application to three-dimensional numerical simulation of segmented chip formation mechanisms in orthogonal cutting, Journal of Manufacturing Processes 73 (2022) 149–163.

[11] A. Vovk, J. Sölter, B. Karpuschewski, Finite element simulations of the material loads and residual stresses in milling utilizing the CEL method, Procedia CIRP 87 (2020) 539–544.

[12] M. Hardt, T. Bergs, Three Dimensional Numerical Modeling of Face Turning Using the Coupled-Eulerian-Lagrangian Formulation, Procedia CIRP 102 (2021) 162–167.

[13] S. N. Melkote, W. Grzesik, J. Outeiro, J. Rech, V. Schulze, H. Attia, P.-J. Arrazola, R. M'Saoubi, C. Saldana, Advances in material and friction data for modelling of metal machining, CIRP Annals 66 (2017) 731–754.

[14] G. Johnson, W. Cook, A constitutive model and data for metals subjected to large strains, high strain rates and high temperatures, in: Proc. 7th International Symposium on Ballistics, volume 21, The Hague, The Netherlands, pp. 541–547.

[15] M. Calamaz, D. Coupard, F. Girot, A new material model for 2D numerical simulation of serrated chip formation when machining titanium alloy Ti–6Al–4V, International Journal of Machine Tools and Manufacture 48 (2008) 275–288.

[16] T. Özel, T. Altan, Determination of workpiece flow stress and friction at the chip–tool contact for high-speed cutting, Int J Mach Tools Manuf 40 (2000) 133–152.

[17] A. Shrot, M. Bäker, Determination of Johnson–Cook parameters from machining simulations, Comput Mater Sci 52 (2012) 298–304.

[18] F. Klocke, D. Lung, S. Buchkremer, I. S. Jawahir, From Orthogonal Cutting Experiments towards Easy-to-Implement and Accurate Flow Stress Data, Materials and Manufacturing Processes 28 (2013) 1222–1227.

[19] P. Bosetti, C. Maximiliano Giorgio Bort, S. Bruschi, Identification of Johnson–Cook and Tresca's Parameters for Numerical Modeling of AISI-304 Machining Processes, J Manuf Sci Eng 135 (2013).

[20] B. Denkena, T. Grove, M. A. Dittrich, D. Niederwestberg, M. Lahres, Inverse Determination of Constitutive Equations and Cutting Force Modelling for Complex Tools Using Oxley's Predictive Machining Theory, Procedia CIRP 31 (2015) 405–410.

[21] T. Bergs, M. Hardt, D. Schraknepper, Determination of Johnson-Cook material model parameters for AISI 1045 from orthogonal cutting tests using the Downhill-Simplex algorithm, Procedia Manuf 48 (2020) 541–552.

[22] M. Hardt, D. Schraknepper, T. Bergs, Investigations on the Application of the Downhill-Simplex-Algorithm to the Inverse Determination of Material Model Parameters for FE-Machining Simulations, Simulation Modelling Practice and Theory 107 (2021) 102214.

[23] B. Stampfer, G. González, E. Segebade, M. Gerstenmeyer, V. Schulze, Material parameter optimization for orthogonal cutting simulations of AISI4140 at various tempering conditions, Procedia CIRP 102 (2021) 198–203.

[24] M. Hardt, D. Jayaramaiah, T. Bergs, On the Application of the Particle Swarm Optimization to the Inverse Determination of Material Model Parameters for Cutting Simulations, Modelling 2 (2021) 129–148.

[25] N. Kugalur Palanisamy, E. Rivière Lorphèvre, M. Gobert, G. Briffoteaux, D. Tuyttens, P.-J. Arrazola, F. Ducobu, Identification of the Parameter Values of the Constitutive and Friction Models in Machining Using EGO Algorithm: Application to Ti6Al4V, Metals 12 (2022) 976.

[26] O. Pantalé, P. Tize Mha, A. Tongne, Efficient implementation of non-linear flow law using neural network into the Abaqus Explicit FEM code, Finite Elements in Analysis and Design 198 (2022) 103647.

[27] S. Seo, O. Min, H. Yang, Constitutive equation for Ti–6Al–4V at high temperatures measured using the SHPB technique, Int J Impact Eng 31 (2005) 735–754.

[28] F. Ducobu, E. Rivière-Lorphèvre, E. Filippi, On the importance of the choice of the parameters of the Johnson-Cook constitutive model and their influence on the results of a Ti6Al4V orthogonal cutting model, Int J Mech Sci 122 (2017) 143–155.

[29] GRANTA EduPack 2020, Granta Design Limited, 2020.

[30] N. Milošević, I. Aleksic, Thermophysical properties of solid phase Ti-6Al-4V alloy over a wide temperature range (2012).

[31] J. Rech, P. J. Arrazola, C. Claudin, C. Courbon, F. Pusavec, J. Kopac, Characterisation of friction and heat partition coefficients at the tool-work material interface in cutting, CIRP Annals 62 (2013) 79–82.

[32] O. Pantalé, Coefficients of an ANN constitutive flow law of a Ti6-Al-4V material for dynamic applications, Zenodo (2022).

[33] L. Wang, H. Long, Investigation of material deformation in multi-pass conventional metal spinning, Materials & Design 32 (2011) 2891–2899.

[34] F. Ducobu, E. Rivière-Lorphèvre, E. Filippi, On the introduction of adaptive mass scaling in a finite element model of Ti6Al4V orthogonal cutting, Simulation Modelling Practice and Theory 53 (2015) 1–14.

[35] M. Sima, T. Özel, Modified material constitutive models for serrated chip formation simulations and experimental validation in machining of titanium alloy Ti–6Al–4V, International Journal of Machine Tools and Manufacture 50 (2010) 943–960.

[36] F. Ducobu, E. Rivière-Lorphèvre, E. Filippi, Material constitutive model and chip separation criterion influence on the modeling of Ti6Al4V machining with experimental validation in strictly orthogonal cutting condition, International Journal of Mechanical Sciences 107 (2016) 136–149.

[37] Y. Karpat, Temperature dependent flow softening of titanium alloy Ti6Al4V: An investigation using finite element simulation of machining, Journal of Materials Processing Technology 211 (2011) 737–749.

[38] Y. C. Zhang, T. Mabrouki, D. Nelias, Y. D. Gong, Chip formation in orthogonal cutting considering interface limiting shear stress and damage evolution based on fracture energy approach, Finite Elements in Analysis and Design 47 (2011) 850–863.

Appendix A. Coefficients of the ANN 3-9-7-1-sig

In this Appendix, we present the values obtained after the training phase of an ANN containing 9 neurons in the first hidden layer and 7 neurons in the second hidden layer.

The training of the neural network was performed using a data set containing 3 430 data points defined by:

- 70 values for $\varepsilon^p \in [0.0, 3.0]$, so that $[\varepsilon^p]_{min} = 0$ and $[\varepsilon^p]_{max} = 3$.
- 7 plastic strain rates $\dot{\varepsilon}^p \in [1, 10, 50, 500, 5\,000, 50\,000, 500\,000]$, so that $[\ln(\dot{\varepsilon}^p)]_{min} = 0$ and $[\ln(\dot{\varepsilon}^p)]_{max} = 13.12236$. [FD:] Add units to values?

- 7 temperatures $T \in [293, 400, 500, 700, 900, 1\,200, 1\,500]$, so that $[T]_{min} = 293$ and $[T]_{max} = 1\,500$. [FD:] Add units to values?

Stresses in the training dataset ranges from $[\sigma^y]_{min} = 171.44$ to $[\sigma^y]_{max} = 2606.12$. The results of the training process are given below for quantities W_1, W_2, $\overrightarrow{w}$, $\overrightarrow{b_1}$, $\overrightarrow{b_2}$ and b.

$$\mathsf{W}_1 = \begin{bmatrix} -0.87229 & -0.47675 & -1.50771 \\ -0.95762 & -0.25619 & 1.65222 \\ -10.61660 & 0.22003 & -0.11539 \\ 3.67883 & 0.37146 & -1.51069 \\ -63.39468 & 0.15466 & -0.95431 \\ 0.54807 & 0.25959 & -5.44355 \\ -1.33883 & 0.36089 & -1.66735 \\ -0.68125 & 1.02121 & 0.34242 \\ 0.08740 & 0.18764 & -41.32542 \end{bmatrix}$$

$$\mathsf{W}_2^T = \begin{bmatrix} 1.66285 & -0.59645 & -3.17333 & 0.20706 & 1.18760 & 2.01250 & -0.82147 \\ -0.26237 & -2.50330 & -1.45941 & -1.59833 & 4.05169 & -1.21146 & 1.05610 \\ -0.12958 & 0.67119 & -5.85989 & -2.55061 & 4.85245 & 4.31876 & 3.24070 \\ -2.12890 & 0.68296 & 0.71183 & 0.81706 & -0.09405 & 0.34919 & -1.41223 \\ 2.33631 & -0.08089 & 14.65789 & 0.12531 & 23.66363 & 2.55872 & 2.15338 \\ 0.11567 & 1.77629 & -1.80448 & 0.77825 & -1.58254 & 1.90442 & 1.23152 \\ 1.49265 & 0.41821 & -3.53803 & -0.48705 & -0.23671 & 0.75887 & -0.37441 \\ 0.95990 & 0.69041 & 0.43870 & 0.28393 & -1.40101 & -0.64569 & -0.38964 \\ 5.89937 & -0.13015 & 2.99264 & 1.78534 & -3.90189 & 1.17494 & -3.78854 \end{bmatrix}$$

$$\overrightarrow{w} = \begin{bmatrix} 0.34701 \\ 1.42079 \\ -0.96564 \\ 0.62467 \\ -0.56322 \\ 0.40960 \\ -0.42810 \end{bmatrix}$$

$$\overrightarrow{b_1} = \begin{bmatrix} 2.57141 \\ 0.22673 \\ -1.16985 \\ -0.11246 \\ -0.82210 \\ -2.13264 \\ 0.78794 \\ 1.20434 \\ -3.48681 \end{bmatrix}$$

$$\overrightarrow{b_2} = \begin{bmatrix} -0.36566 \\ -1.14445 \\ -0.79065 \\ -0.50670 \\ 1.30136 \\ 0.04521 \\ -0.29995 \end{bmatrix}$$

$$b = 0.04213$$